UC San Diego
UC San Diego Previously Published Works

Title

Self-branched α-MnO2/δ-MnO2 heterojunction nanowires with enhanced pseudocapacitance

Permalink

https://escholarship.org/uc/item/4vb7r4rg

Journal

Materials Horizons, 4(3)

ISSN

2051-6347

Authors

Zhu, C
Yang, L
Seo, JK
et al.

Publication Date

2017

DOI

10.1039/c6mh00556j

Peer reviewed

COMMUNICATION

Self-branched α-MnO₂/δ-MnO₂ heterojunction nanowires with enhanced pseudocapacitance†

Changrong Zhu,[ab] Lu Yang,[a] Joon Kyo Seo,[a] Xiao Zhang,[c] Shen Wang,[a] JaeWook Shin,[a] Dongliang Chao,[b] Hua Zhang,[c] Ying Shirley Meng*[a] and Hong Jin Fan*[b]

Despite the extensive research on MnO₂ as a pseudocapacitor electrode material, there has been no report on heterostructures of multiple phase MnO₂. Here we report the combination of two high-capacitance phases of MnO₂, namely, α-MnO₂ nanowires and δ-MnO₂ ultrathin nanoflakes, to form a core-branch heterostructure nanoarray. This material and structure design not only increases the mass loading of active materials (from 1.86 to 3.37 mg cm²), but also results in evident pseudocapacitance enhancement (from 28 F g⁻¹ for pure nanowires to 178 F g⁻¹ for heterostructures at 5 mV s⁻¹). The areal capacitance is up to 783 mF cm⁻² at 1 mV s⁻¹. Upon 20 000 cycles, the heterostructure array electrode still delivers a reversible capacitance above 100 F g⁻¹ at 4.5 A g⁻¹. Kinetic analysis reveals that capacitances due to both capacitive and diffusion controlled processes have been enlarged for the self-branched heterostructure array. This work presents a new route to improve the electrochemical performance of MnO₂ as a binder-free super-capacitor electrode.

Conceptual insights

The performance of electrochemical energy storage devices relies largely on the scrupulous design of nanoarchitectures and smart hybridization of active materials. Nanoarray electrodes are particularly investigated as a power source in microelectronic devices, which require high rates, high areal capacity/capacitance and long cycle stability. MnO₂ has been the paradigm pseudo-capacitive material that is promising for practical applications. It has many crystal phases, among which α-MnO₂ and δ-MnO₂ have relatively high capacitance. Numerous studies have shown that the crystal phase is an important factor for the electrochemical property of an electrode material. We constructed a bi-phase hetero-structure nanoarray electrode by growing thin nanoflakes of δ-MnO₂ onto α-MnO₂ nanowire cores. This not only increases the mass loading to the highest value compared to the literature, but also significantly increased the areal capacitance. Interestingly, the capacitance originates from both the well-known pseudocapacitive process and Li-ion diffusion processes due to the large lattice spacing of the δ-phase nanosheets.

Introduction

There is tremendous demand for energy storage devices that exhibit both high energy density and greater power density than the state-of-the-art lithium ion batteries.[1–4] As a typical high power candidate, supercapacitors can also deliver energy density comparable to batteries by utilizing high-capacitance electrode materials according to the equation $E = \frac{1}{2}CV^2$, where E is energy stored in the device, C is capacitance and V is the open-circuit potential.[5–10] For supercapacitors, the aim is to boost the energy density without sacrificing the high power capability. In this regard, transition metal oxides with generally high theoretical

capacitances are of high pertinence. Manganese dioxide (MnO₂) is one of the typical pseudo-capacitive materials.[11–14] In an aqueous electrolyte, the redox reaction between MnO₂ and cations follows $MnO_2 + M^+ + e^- \Leftrightarrow MnOOM$ (M⁺ stands for H₃O⁺ or alkali cations such as K⁺, Na⁺ and Li⁺),[15–18] which delivers a theoretical pseudocapacitance of ~1370 F g⁻¹. Furthermore, because of the multi-modality of the octahedral [MnO₆] basic unit linkage, MnO₂ forms a variety of crystal phases (α, β, γ and δ *etc.*).[11,12,14,19–27] In particular, 3D tunneling structures are formed in α (2 × 2 and 1 × 1),[20,21,23] β (1 × 1)[19] and γ (2 × 1)[12,27] phases whereas δ-MnO₂ possesses a 2D layered structure.[14,22,24–26] Accordingly, the tunnel sizes in α-MnO₂ and δ-MnO₂ are 0.46 nm and 0.7 nm, respectively, both much larger than that in β-MnO₂ (0.23 nm).[11,12,19,20] Previous study has shown that α-MnO₂ and δ-MnO₂ are of higher capacitance than the β and γ counterparts.[28] Hence, utilizing α-MnO₂ and δ-MnO₂ as supercapacitor electrodes should be beneficial for achieving high capacitance.

So far there is vast literature on supercapacitive MnO₂ in which capacitance values close to the theoretical quantity of 1370 F g⁻¹ have been reported.[13,14,21,23,25,29–34] However, most of these studies utilized a rather thin MnO₂ film with mass loadings

ᵃ *Department of NanoEngineering, University of California San Diego, La Jolla, California 92093-0448, USA. E-mail: shmeng@ucsd.edu*

ᵇ *School of Physical and Mathematical Sciences, Nanyang Technological University, 637371, Singapore. E-mail: fanhj@ntu.edu.sg*

ᶜ *Center for Programmable Materials, School of Materials Science and Engineering, Nanyang Technological University, 639798, Singapore*

† Electronic supplementary information (ESI) available. See DOI: 10.1039/c6mh00556j

less than 0.5 mg cm^{-2}. Therefore, the total capacitance (in units of F) and amount of charge (in units of C) are small, which will not meet certain applications that require high areal and/or volumetric capacitance. On the other hand, active materials directly grown on current collectors are regarded as important to the construction of high energy density electrodes. Binders (such as PVDF) and conductive agents (such as acetylene black) lower the overall capacitance of the entire electrode because they reduce the ratio of active materials. So far, growing single-phase MnO$_2$ nanostructures directly on a conductive substrate such as graphene, graphene foam, carbon nanotubes or carbon cloth has been reported by electrodeposition or hydrothermal methods.[26,27,34–38] These array electrodes are all based on single-phase MnO$_2$ and the carbon materials do not contribute to the capacitance. There is no report yet on multiple phase hetero-structures for high-capacitance electrodes.

A previous study demonstrated a synergistic effect between anatase and TiO$_2$-B in bi-phase TiO$_2$ nanosheets, which accounts for a capacity increase for lithium ion storage.[39] Inspired by this, we intend to enhance the capacitance of MnO$_2$ by optimizing the phase combination in the array structure. Our mature synthesis capability enables us to construct core-branch nanostructures with a mass loading up to 3.37 mg cm^{-2}. In the self-branched hetero-structures, the intrinsic merits of large capacitance of both phases can be more efficiently utilized. Based on the above design, the core-branch electrode indeed shows a much higher specific capacitance than single-phase nanowires at all different scan rates. In addition, it exhibits high capacitance retention ($\sim$86%) after a 20 000 cycles @ 4.5 A g^{-1}. These properties (cycling stability and capacitance) are considered superior among all the binder-free MnO$_2$ capacitive electrodes.[36–38]

Experimental

Material preparation

Carbon cloth containing highly ordered weaved carbon fibers with diameters $\sim$5 µm was used as a current collector and conductive substrate to support the electrode active material. The carbon cloth was purchased from Cetech Tai Wan. The thickness as provided by the manufacturer is $\sim$300 µm. The carbon cloth was treated in air plasma (room temperature, 230 psi for 10 min) to make the surface hydrophilic. Then MnO$_2$ nanowires were grown through a hydrothermal synthesis. In detail, 0.25 g KMnO$_4$, 0.048 g Fe$_2$(SO$_4$)$_3$ and 18 µl concentrated H$_2$SO$_4$ were mixed in 80 ml distilled water with magnetic stirring at room temperature for 20 min. The resulting solution was transferred into a 50 ml autoclave, which was kept in a box furnace under 150 °C for 6 h. Then the obtained materials were thoroughly washed with distilled water and dried in an electrical oven (80 °C, 8 h). Afterwards, in order to grow the MnO$_2$ branches, the samples underwent a second hydrothermal process. The procedure is similar as above except for the solution (herein pure KMnO$_4$ 0.2844 g) and the reaction conditions (160 °C, 1 h). Finally, both the as-synthesized MnO$_2$ nanowires and MnO$_2$ core-branch sample were annealed in Ar at 250 °C for 2 h.

Structural and morphology characterization

The crystal structures of the samples were identified using XRD (RigakuD/Max-2550 with Cu Kα radiation) and Raman spectroscopy (Renishaw InVia Raman microscope). Raman spectra were recorded using a 633 nm laser excitation source and a ×50 objective lens. The exposure time was limited to 30 s with 5 accumulations to minimize the beam damage. Different spots across the sample were examined to confirm the consistency of the results. Fits of Raman spectra were performed using PeakFit software (version 4.12) automatically with the assumptions of linear background and that all Raman bands have a Lorentz line shape. The morphology of all the samples was examined using an Ultra-High Resolution Scanning Electron Microscope (FEI XL30 SFEG UHR SEM) at 10 kV and TEM/HRTEM (JEOL JEM-2100F) operating at 200 kV. AFM measurements were conducted using a Veeco Scanning Probe Microscope in tapping mode. The surface areas of the samples were determined by gas adsorption analyses using Quantachrome Instruments Autosorb-iQ (Boynton Beach, Florida USA, gas purity $\sim$99.99%, samples were outgassed at 150 °C for 6 h for activation). The specific surface area was calculated using the Brunauer–Emmett–Teller (BET) model. The pore size distribution was determined using the Barrett–Joyner–Halenda (BJH) method.

Electrochemical tests and mass determination

The electrochemical tests were conducted with a standard three-electrode testing system where the electrode materials (1 × 1 cm^2) acted as a working electrode, Pt as a counter electrode and Ag/AgCl as a reference electrode in 1 M LiCl electrolyte (Salartron). The active material mass loading was determined by weighing the samples after each step of the synthesis procedure using a high-precision balance (0.001 mg). The mass loading of the self-branched MnO$_2$ electrode on the carbon cloth is about 3.37 mg cm^{-2} and it is about 1.86 mg cm^{-2} for the pure MnO$_2$ nanowire sample.

Calculations of specific capacitance

The specific gravimetric capacitances (C_m) are calculated based on the CV curves according to the following equations:

$$C_m = \frac{Q}{\Delta U \times m} = \frac{\int I_m \mathrm{d}U}{2v\Delta U}$$

where C_m (F g^{-1}) is the specific capacitance, Q (C) is the average charge, ΔU (V) is the potential window, v (V s^{-1}) is the scan rate, and I_m (A g^{-1}) is the gravimetric current of the working electrode (i.e. the vertical coordinate of the CV curve). There is a factor 2 because one CV cycle includes charge and discharge process, and the integral contains the charge of these two processes.

Results and discussion

Fig. 1 illustrates the synthesis process of the resulting self-branched MnO$_2$ (SBM) electrode with a 3D tunneled structure in its core and 2D layered structures in the branches, formed by the stacking of different [MnO$_6$] octahedral basic units. In the first
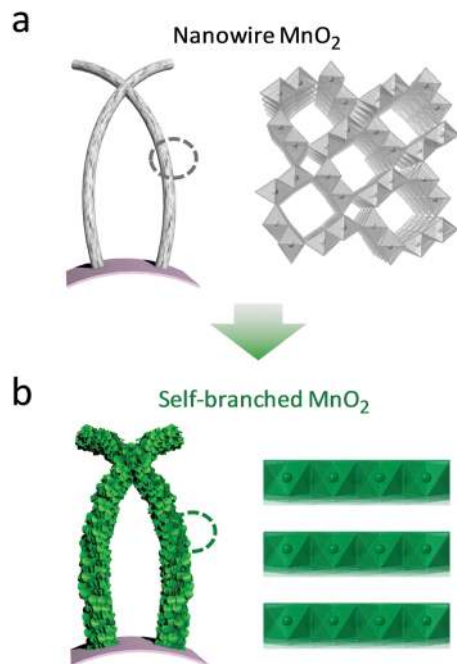
Fig. 1 Illustration of electrode design. (a) Alpha-MnO_2 (with 2×2 and 1×1 channels) nanowires on carbon cloth; (b) self-branched MnO_2 electrode formed after delta-MnO_2 (with a layered structure) flakes were decorated onto the alpha-MnO_2 nanowires.

hydrothermal process, alpha-phase nanowire MnO_2 (NWM) is designed to grow directly on a piece of the conductive carbon cloth substrate and acts as the backbone (Fig. 1a). Then, the entire layout is completed with delta-phased MnO_2 nanoflakes fully anchored to the MnO_2 nanowire skeleton (Fig. 1b).

We unveiled the morphology of the electrode materials under a scanning electron microscope (SEM). After plasma treatment in air for 10 min, the carbon cloth surface becomes hydrophilic. This is a necessity step for the nucleation and growth of MnO_2

in this study (as well as of course other active materials in hydrothermal growth). The first-stage hydrothermal synthesis results in MnO_2 nanowire arrays that grow homogeneously on the carbon cloth (Fig. 2a). The length of the nanowires is $\sim 5\ \mu m$, which to the best of our knowledge is the longest among all the reported 1D MnO_2 fabricated through solution based methods.[23,40] A possible reason for this different sample morphology is that they were grown under the highly concentrated heating conditions of the box furnace whereas traditional hydrothermal growth is usually conducted in an electric oven. Higher magnification SEM images (Fig. 2b), together with atomic force microscopy (Fig. 2c and Fig. S1, ESI†), further confirm the solid nanowire morphology. After the second hydrothermal procedure, the nanowire skeleton is well preserved (Fig. 2d) and uniformly decorated with thin flakes, forming a nanoflake@nanowire core-branch structure (Fig. 2e). To tighten the connection of the nanoarrays to the carbon cloth substrate, the sample after hydrothermal growth was further annealed in an Ar atmosphere at 250 °C for 2 h. As seen from Fig. 2f, the final core-branch array structure is retained.

In order to confirm the two phases in the core-branch electrode, we first looked at X-ray diffraction (XRD) results. Because of the similar interlayer spacing values of the MnO_2 alpha and delta phases (as shown by the calculated spectra), many of the diffraction peaks appear at the same position, as seen in Fig. 3a. For example, α-MnO_2(110) and δ-MnO_2(001) locate at $2\theta = 12.6°$; α-MnO_2(400) and δ-MnO_2(110) locate at $2\theta = 36.3°$, α-MnO_2(411) and δ-MnO_2(−112) locate at $2\theta = 50.3°$, and α-MnO_2(002) and δ-MnO_2(−312) locate at $2\theta = 65.3°$ (α-MnO_2 ref. JCPDS #44-0141; δ-MnO_2 ref. JCPDS #42-1317).[14,20–26,30] Therefore, the key to differentiating these two phases is the δ-MnO_2(002) peak located at $2\theta = 25.4°$. Unfortunately, this peak overlaps with the main peak of carbon from the substrate.

We seek further verification with Raman spectroscopy, considering that manganese dioxide is very Raman active because
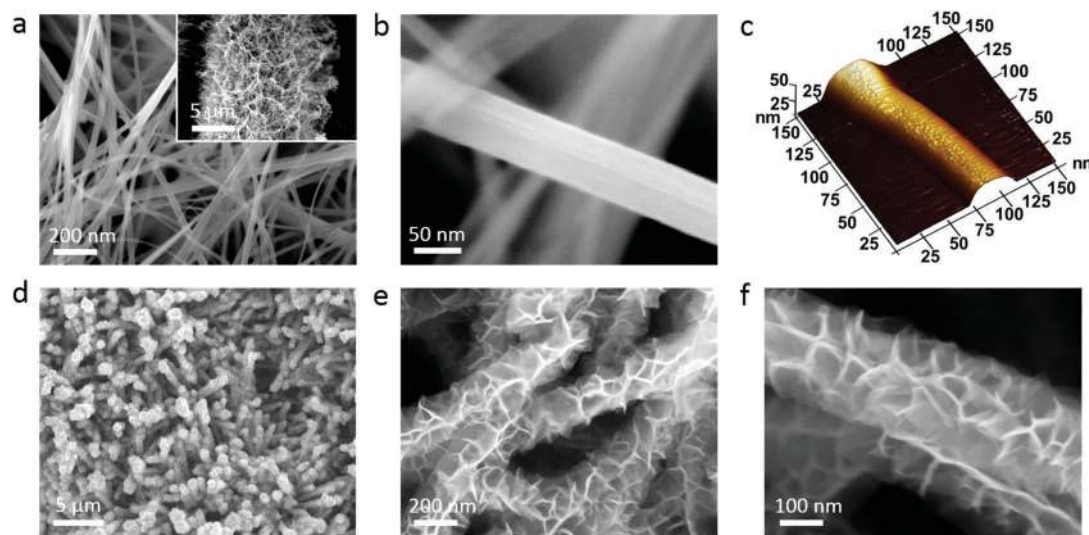

Fig. 2 Morphology. SEM images of (a and b) NW MnO_2. Inset of a is the nanowire under low magnification showing the homogeneous distribution of the wires on the carbon fiber. (c) AFM 3D image of a single nanowire. (d and e) The as-synthesized SB MnO_2 electrode and (f) after annealing.
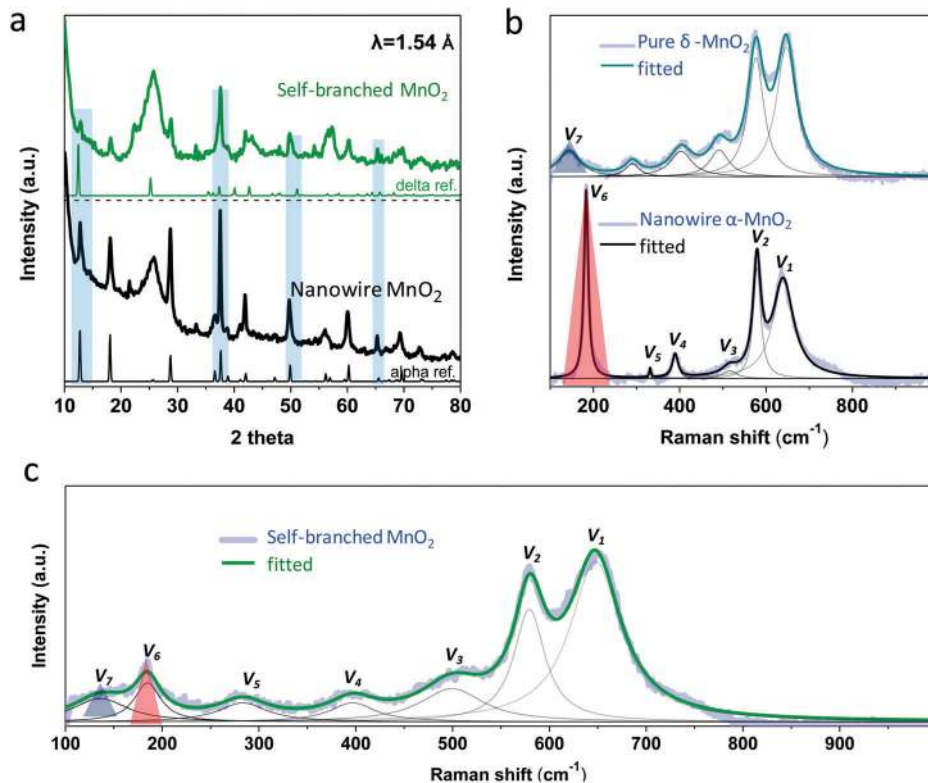
Fig. 3 Crystal structure. (a) XRD spectra of the NWM and SBM electrodes. The vertical bars indicate the common peaks appearing in both samples. Raman spectra of (b) the alpha (nanowire) and delta phase (controlled sample) MnO_2 and (c) the SBM electrode. The fitted peak positions are listed in Table S1 in the ESI.†

of its short-range ordering crystalline structure. According to the group theoretical calculations, alpha-MnO_2 ($I4/m$ space group) has fifteen vibration modes ($6A_g + 6B_g + 3E_g$) while delta-MnO_2 ($C2/m$ space group) has nine Raman active modes ($3A_g + 6B_g$). Because of the low polarizabilities of some vibration modes and the overlapping of incompletely resolved modes, we have to differentiate alpha and delta phase MnO_2 at their low frequency regions.[41–43] Based on previous research, we fit the Raman spectra of α- and δ-manganese dioxide with Lorentz fitting which basically locates seven strong and weak Raman bands.[44,45] The fitted results (Fig. 3b) point out the difference between the α- and δ-MnO_2 clearly because α-MnO_2 monopolizes the V_6 peak (183 cm^{-1}) while δ-MnO_2 produces a broad V_7 peak (130–150 cm^{-1}). Because of the high similarities, α- and δ-MnO_2 share the Raman peaks from V_1 to V_5 (see the peak positions listed in Table S1 and detailed Raman fitting analysis in the ESI†). All the peaks are detected in SBM (Fig. 3c) including the key different near region peaks of V_6 and V_7. Thus the SBM can be confirmed to contain both α- and δ-MnO_2.

To provide more evidence of the morphology and crystal structure, transmission electron microscopy (TEM) characterization was conducted for both MnO_2 electrode materials. The low magnification TEM images confirmed the nanowire (Fig. 4a) and nanowire@nanoflake core–shell (Fig. 4c) structure of the NWM and SBM, respectively. Regarding the pure MnO_2 nanowires, the high resolution TEM characterization exhibits the (110) lattice of α-MnO_2 (d = 6.9 Å) in Fig. 4b, corresponding well

with the XRD data in Fig. 3a. Furthermore, the fast Fourier transform (FFT) image generated from the same area demonstrates its single crystalline property (Fig. 4b inset). Moreover, in the HRTEM images of the SBM sample, typical planes of the δ-MnO_2-(110) (d = 2.5 Å), δ-MnO_2-(200) (d = 2.6 Å) and δ-MnO_2-(−114) lattice (d = 1.5 Å) are identified on the edge region (Fig. 4d), confirming the existence of δ-MnO_2 in the SBM electrode. Meanwhile, the TEM element mapping shows that the homogeneous distributions of Mn and O match well with the dark-field image of the SBM profile (Fig. 4e). Hence, the co-existence of two MnO_2 phases in the SBM structure is further exhibited. Therefore, both the α-MnO_2@δ-MnO_2 core-branch and the pure α-MnO_2 nanowire structures are verified.

Nanoflakes grown on the nanowire can increase the active material mass loading and generally ensure an improved surface area of the electrode. To confirm this, a gas adsorption method was employed to characterize the specific surface area (Fig. S2, ESI†). Under the Brunauer–Emmett–Teller (BET) model, the surface area of the SBM nanostructure is calculated to be 60.7 m^2 g^{-1}, which is six times that of NWM (10.2 m^2 g^{-1}). The 2 × 2 tunnels (0.46 nm) in α-MnO_2 and the layered structure (0.69 nm) of δ-MnO_2 are both beneficial for facilitating ion insertion and transport. Therefore, we foresee that the combination of these two phases can secure an improved rate performance and an increased capacitance.

To evaluate the structure design, the electrochemical properties of the pure α-MnO_2 nanowires and bi-phase core-branch
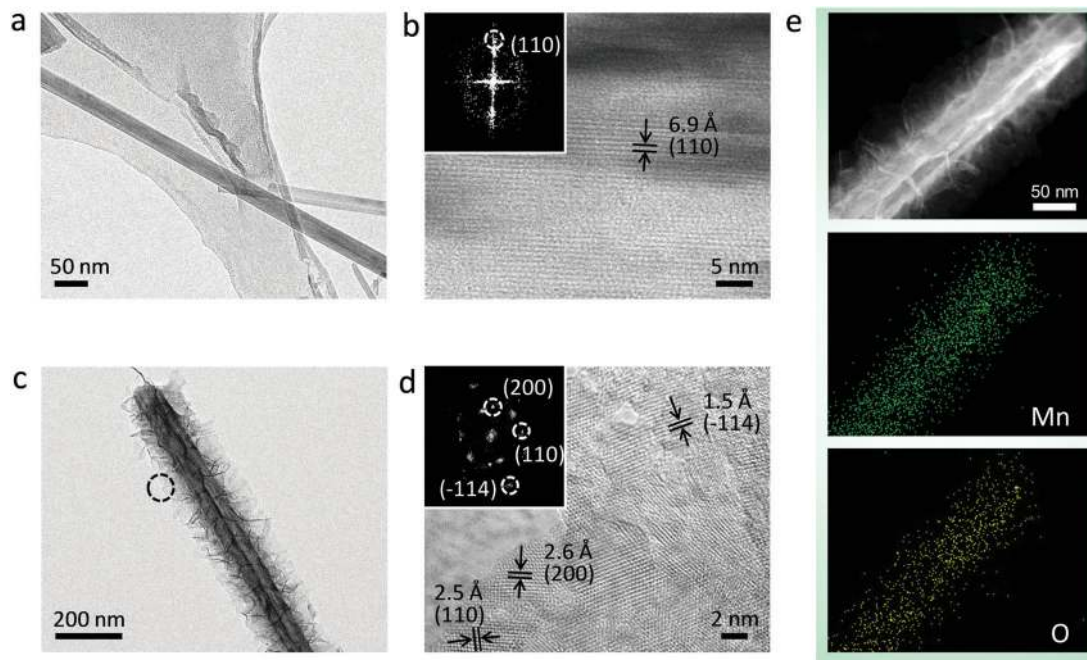
Fig. 4 Morphology and crystal information study with TEM. TEM images of (a) NWM and (c) SBM nanostructures; HRTEM images of (b) NWM and (d) SBM nanostructures, with insets showing the fast Fourier transfer (FFT) generated from the same area; (e) TEM element mapping of a single SBM wire.

electrodes as supercapacitive electrodes are tested for comparison. Both electrodes produce quasi-rectangular-shaped capacitive cyclic voltammetry (CV) curves (Fig. 5a) at 1 mV s^{-1}. The capacitance for the pure MnO_2 nanowires is rather small, as indicated by the low current density value of the CV curves (Fig. S3a, ESI†). In contrast, after the decoration with MnO_2 nanoflakes, the specific capacitances are drastically increased as seen from the comparison in Fig. 5a. Moreover, when the scan speed increases from 2 to 20 mV s^{-1}, the SBM still exhibits quasi-rectangular shaped CV curves (Fig. 5b), manifesting the dominating capacitive behavior. It is worth mentioning that the capacitance increase of the SBM electrode compared to the pure nanowire electrode also occurs consistently at all different scan speeds (from 1, 2, 5, 10, to 20 mV s^{-1}). Their corresponding values obtained from the CV curves are (SBM *vs.* α-MnO_2 nanowire): 232 *vs.* 32 F g^{-1}, 208 *vs.* 28 F g^{-1}, 179 *vs.* 25 F g^{-1}, 152 *vs.* 23 F g^{-1} and 116 *vs.* 22 F g^{-1} (Fig. 5b and Fig. S3a, ESI†). The galvanostatic charge–discharge curves of both electrodes are in a triangular shape (Fig. 5c and Fig. S3b, ESI†), further verifying the dominating capacitive behavior. The coulombic efficiency (C.E.) calculated from charge/discharge curves (Fig. S5, ESI†) shows that the C.E. of both the SBM and NWM electrodes are above 95% under various current densities. The obvious capacitance loss at 1 A g^{-1} could be due to the irreversible Li$^+$ insertion. At rates higher than 3 A g^{-1}, the insignificant capacitance loss is proposed to be related to the oxygen evolution reaction. Upon prolonged cycling up to 20 000 cycles, the core-branch nanowire electrode shows nearly overlapping charge and discharge capacitances with reasonable stability (retention ∼86%, see Fig. 5e). This retention is somewhat inferior to that of the pure MnO_2 nanowire electrode (∼98%), but the capacity values are always significantly higher (*e.g.*, 100 F g^{-1} *versus* 20 F g^{-1}).

To better understand the capacitance enhancement effect of combining these two phases, δ-MnO_2 nanoflakes were also synthesized on carbon paper for comparison (data are presented in Fig. S4, ESI†). The specific capacitances calculated from the CV curves were plotted together with the pure alpha MnO_2 nanowires and the SBM electrode. It is clear that the SBM composite electrode exhibits higher capacitance than both MnO_2 nanowires and nanoflakes at different scan speeds (Fig. S4b, ESI†), demonstrating the advantage of combining these two phases into a core-branch architecture. We ascribe this capacitance enhancement essentially to the increased surface area and also a synergistic effect. The alpha and delta phase MnO_2 may have a poor-defined crystallographic interface as they may diffuse into the lattice of each other and cause lattice defects, which is common for heterostructures. The defects will lead to further exposure of electrochemical active sites and to increased capacitance, similar to previous studies.[39,46,47]

For powder-packed electrodes, an increase in material loading will generally lead to a reduction in the specific capacitance by lowering the electrode utilization efficiency. On the other hand, nanoscale electrode materials exhibit both a diffusion-controlled current and a pure capacitive one; the enlarged surface area and shortened diffusion distance may lead to fast kinetics thus contributing to capacitive current. In our case, marriage of the nanoflakes and nanowires forming a 3D hierarchical array structure does not eliminate effective interfaces between the electrode and electrolytes; instead, it would provide fast ion transport for the surface redox reactions. This will facilitate ion diffusion and lead to higher capacitive current than the pure nanowire electrode. To verify this, we calculated the capacitances based on the CV curves obtained from various scan speeds following
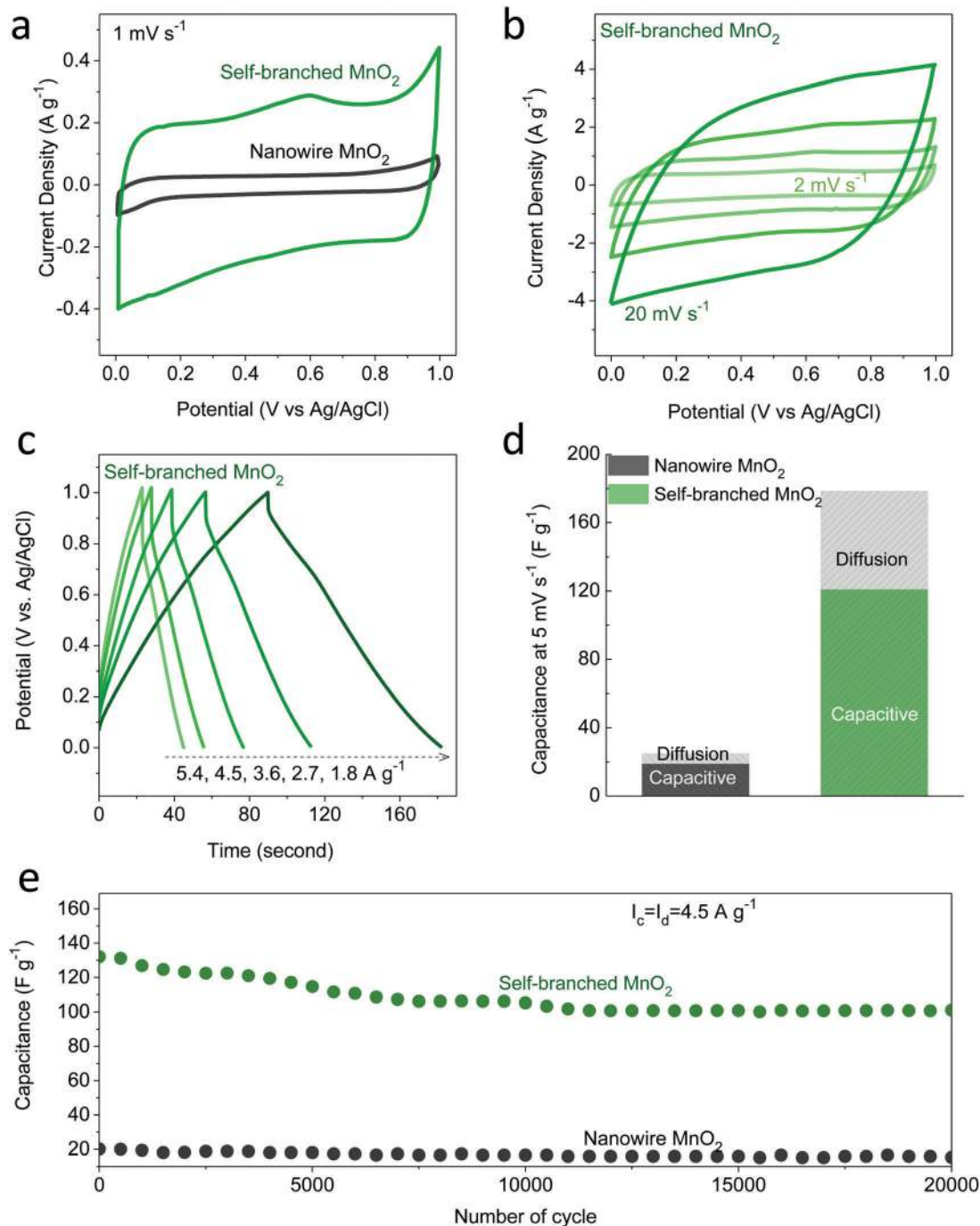
Fig. 5 Electrochemical properties. (a) CV curve comparison of NWM and SBM nanostructures at 1 mV s^{-1}; (b) CV curves of the SBM nanostructure at different scan speeds; (c) charge–discharge curves of the SBM nanostructure at a varied current density; (d) capacitance contribution calculations of MnO$_2$ electrodes at 5 mV s^{-1}. (e) Cycling performance of NWM and SBM nanostructures in 20 000 cycles under 4.5 A g^{-1}.

the standard method.[48–56] One example at 5 mV s^{-1} is selected for analysis (Fig. 5d and Fig. S6, ESI†). The capacitance contribution in the SBM electrode from capacitive behavior is nearly ten times that of the NWM electrode ($\sim$120 vs. 19 F g^{-1}). Similar results have been obtained for other scan speeds, i.e., $\sim$8 times increase in capacitive process induced capacitance. In addition, we also notice the enhancement in capacitance due to the battery insertion process, in which Li ions diffuse swiftly and reversibly

into lattice channels. For example, in Fig. 5d the "diffusion contributed capacitance" increases from 9 to 58 F g^{-1}. This additional capacitance can also be ascribed to the δ-MnO$_2$ nanoflake branches, which have well-defined diffusion channels for Li ions with a 0.69 nm lattice spacing. All in all, the above results demonstrate clearly that the judicious combination of the bi-phase MnO$_2$ nanocrystals has increased the entire mass loading of MnO$_2$ without sacrificing the capacitance; instead, the total
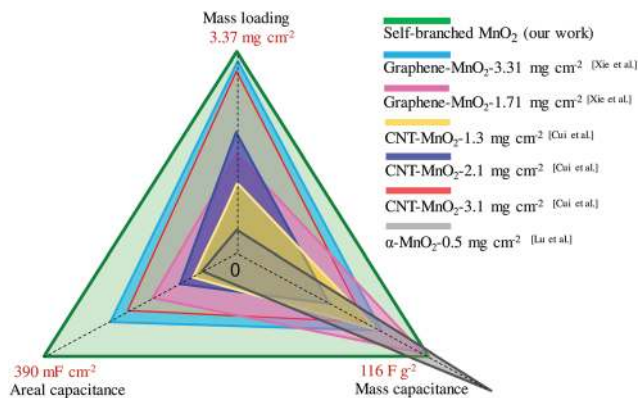
Fig. 6 Capacitance comparison with previous studies considering mass loading. All the capacitance values were obtained at a scan rate of 20 mV s^{-1}.

capacitance due to both capacitive and diffusion processes has been enlarged.

To benchmark our result, the stereogram of gravimetric capacitance and areal capacitance against mass loading is plotted in Fig. 6 in comparison to previous work on MnO$_2$ nanostructure array electrodes (their values are also tabulated in Table S2, ESI†).[13,23,37,57] The comparison shows that our SBM electrode has the highest areal capacitance and also relatively high gravimetric capacitance despite the highest mass loading. This is very encouraging as MnO$_2$ is one of the promising materials for supercapacitor applications. It is optimistic that such bi-phase MnO$_2$ synthesized into other nanostructures, such as core–shell hollow particles and particle-anchored nanoflakes, may also deliver superior performance in supercapacitive charge storage.

Conclusions

To sum up, for the first time we have realized a bi-phase self-branched MnO$_2$ nanoarray structure, which is proven to be effective in boosting the MnO$_2$ capacitance. The α-MnO$_2$ nanowire cores and the δ-MnO$_2$ nanoflake branches have different crystal structures and capacitive properties, and a positive synergistic effect has probably accounted for the drastic capacitance enhancement. The self-branched electrode presents fairly stable cycling with ∼86% capacitance retention in 20 000 cycles. Through kinetic analysis of the charge storage behaviors, we have quantitatively identified that the self-branched electrode exhibits enlarged capacitances due to both capacitive and ion diffusion processes. We ascribe this enhancement to the self-branched configuration with δ-MnO$_2$ thin flakes. This material design paves the way for creating electrodes with high mass loading by utilizing multi-phased metal oxide heterostructures, including but not limited to TiO$_2$ and SnO$_2$.

Acknowledgements

References

1 V. Augustyn, P. Simon and B. Dunn, *Energy Environ. Sci.*, 2014, **7**, 1597–1614.
2 L. Liu, Z. Niu and J. Chen, *Chem. Soc. Rev.*, 2016, **45**, 4340–4363.
3 Y. Wang, Y. Song and Y. Xia, *Chem. Soc. Rev.*, 2016, **45**, 5925–5950.
4 C. Zhu, P. Yang, D. Chao, W. Mai and H. J. Fan, *ChemNanoMat*, 2015, **1**, 458–476.
5 G. Wang, L. Zhang and J. Zhang, *Chem. Soc. Rev.*, 2012, **41**, 797–828.
6 J. Yan, Q. Wang, T. Wei and Z. Fan, *Adv. Energy Mater.*, 2014, **4**, 1300816.
7 A. S. Arico, P. Bruce, B. Scrosati, J.-M. Tarascon and W. van Schalkwijk, *Nat. Mater.*, 2005, **4**, 366–377.
8 B. G. Choi, M. Yang, W. H. Hong, J. W. Choi and Y. S. Huh, *ACS Nano*, 2012, **6**, 4020–4028.
9 S. Faraji and F. N. Ani, *J. Power Sources*, 2014, **263**, 338–360.
10 C. D. Lokhande, D. P. Dubal and O.-S. Joo, *Curr. Appl. Phys.*, 2011, **11**, 255–270.
11 S. Chen, J. Zhu, Q. Han, Z. Zheng, Y. Yang and X. Wang, *Cryst. Growth Des.*, 2009, **9**, 4356–4361.
12 S. Chou, F. Cheng and J. Chen, *J. Power Sources*, 2006, **162**, 727–734.
13 L. Hu, W. Chen, X. Xie, N. Liu, Y. Yang, H. Wu, Y. Yao, M. Pasta, H. N. Alshareef and Y. Cui, *ACS Nano*, 2011, **5**, 8904–8913.
14 J. Liu, J. Jiang, C. Cheng, H. Li, J. Zhang, H. Gong and H. J. Fan, *Adv. Mater.*, 2011, **23**, 2076–2081.
15 O. Ghodbane, J.-L. Pascal and F. Favier, *ACS Appl. Mater. Interfaces*, 2009, **1**, 1130–1139.
16 Y. Liu, X. Miao, J. Fang, X. Zhang, S. Chen, W. Li, W. Feng, Y. Chen, W. Wang and Y. Zhang, *ACS Appl. Mater. Interfaces*, 2016, **8**, 5251–5260.
17 V. Subramanian, H. Zhu, R. Vajtai, P. Ajayan and B. Wei, *J. Phys. Chem. B*, 2005, **109**, 20207–20214.
18 J. Yan, Z. Fan, T. Wei, W. Qian, M. Zhang and F. Wei, *Carbon*, 2010, **48**, 3825–3833.
19 H. Jiang, T. Zhao, J. Ma, C. Yan and C. Li, *Chem. Commun.*, 2011, **47**, 1264–1266.
20 J. Liu, J. Essner and J. Li, *Chem. Mater.*, 2010, **22**, 5022–5030.
21 R. Liu, J. Duay and S. B. Lee, *ACS Nano*, 2010, **4**, 4299–4307.
22 Y. Liu, Y. Qiao, W. Zhang, H. Wang, K. Chen, H. Zhu, Z. Li and Y. Huang, *J. Mater. Chem. A*, 2015, **3**, 7780–7785.

23 W. Xiao, H. Xia, J. Y. H. Fuh and L. Lu, *J. Power Sources*, 2009, **193**, 935–938.

24 C. Xu, Y. Zhao, G. Yang, F. Li and H. Li, *Chem. Commun.*, 2009, 7575–7577.

25 W. Yan, T. Ayvazian, J. Kim, Y. Liu, K. C. Donavan, W. Xing, Y. Yang, J. C. Hemminger and R. M. Penner, *ACS Nano*, 2011, **5**, 8275–8287.

26 X. Zhang, X. Chang, N. Chen, K. Wang, L. Kang and Z.-H. Liu, *J. Mater. Sci.*, 2012, **47**, 999–1003.

27 X. Zhao, L. Zhang, S. Murali, M. D. Stoller, Q. Zhang, Y. Zhu and R. S. Ruoff, *ACS Nano*, 2012, **6**, 5404–5412.

28 S. Devaraj and N. Munichandraiah, *J. Phys. Chem. C*, 2008, **112**, 4406–4417.

29 J. N. Broughton and M. J. Brett, *Electrochim. Acta*, 2004, **49**, 4439–4446.

30 Q. Fan and M. S. Whittingham, *Electrochem. Solid-State Lett.*, 2007, **10**, A48–A51.

31 J.-H. Kim, K. H. Lee, L. J. Overzet and G. S. Lee, *Nano Lett.*, 2011, **11**, 2611–2617.

32 H.-S. Nam, J. S. Kwon, K. M. Kim, J. M. Ko and J.-D. Kim, *Electrochim. Acta*, 2010, **55**, 7443–7446.

33 H. Xia, J. Feng, H. Wang, M. O. Lai and L. Lu, *J. Power Sources*, 2010, **195**, 4410–4413.

34 K. Zhang, X. Han, Z. Hu, X. Zhang, Z. Tao and J. Chen, *Chem. Soc. Rev.*, 2015, **44**, 699–728.

35 W.-Y. Zou, W. Wang, B.-L. He, M.-L. Sun and Y.-S. Yin, *J. Power Sources*, 2010, **195**, 7489–7493.

36 Y. Cheng, S. Lu, H. Zhang, C. V. Varanasi and J. Liu, *Nano Lett.*, 2012, **12**, 4206–4211.

37 Y. He, W. Chen, X. Li, Z. Zhang, J. Fu, C. Zhao and E. Xie, *ACS Nano*, 2012, **7**, 174–182.

38 P. Lv, Y. Y. Feng, Y. Li and W. Feng, *J. Power Sources*, 2012, **220**, 160–168.

39 Q. Wu, J. Xu, X. Yang, F. Lu, S. He, J. Yang, H. J. Fan and M. Wu, *Adv. Energy Mater.*, 2015, **5**, 1401756.

40 H. Pan, Y. Shao, P. Yan, Y. Cheng, K. S. Han, Z. Nie, C. Wang, J. Yang, X. Li, P. Bhattacharya, K. T. Mueller and J. Liu, *Nat. Energy*, 2016, 16039.

41 R. Baddour-Hadjean and J.-P. Pereira-Ramos, *Chem. Rev.*, 2009, **110**, 1278–1319.

42 T. Gao, M. Glerup, F. Krumeich, R. Nesper, H. Fjellvåg and P. Norby, *J. Phys. Chem. C*, 2008, **112**, 13134–13140.

43 C. Julien, M. Massot, R. Baddour-Hadjean, S. Franger, S. Bach and J. Pereira-Ramos, *Solid State Ionics*, 2003, **159**, 345–356.

44 D. Chen, D. Ding, X. Li, G. H. Waller, X. Xiong, M. A. El-Sayed and M. Liu, *Chem. Mater.*, 2015, **27**, 6608–6619.

45 T.-H. Wu, D. Hesp, V. Dhanak, C. Collins, F. Braga, L. J. Hardwick and C.-C. Hu, *J. Mater. Chem. A*, 2015, **3**, 12786–12795.

46 Y. Zheng, Y. Jiao, M. Jaroniec and S. Z. Qiao, *Angew. Chem., Int. Ed.*, 2015, **54**, 52–65.

47 D. Yang, H. Liu, Z. Zheng, Y. Yuan, J.-c. Zhao, E. R. Waclawik, X. Ke and H. Zhu, *J. Am. Chem. Soc.*, 2009, **131**, 17885–17893.

48 V. Augustyn, J. Come, M. A. Lowe, J. W. Kim, P.-L. Taberna, S. H. Tolbert, H. D. Abruña, P. Simon and B. Dunn, *Nat. Mater.*, 2013, **12**, 518–522.

49 R. Li and J. Liu, *Electrochim. Acta*, 2014, **120**, 52–56.

50 J. Yang, S. Muhammad, M. R. Jo, H. Kim, K. Song, D. A. Agyeman, Y.-I. Kim, W.-S. Yoon and Y.-M. Kang, *Chem. Soc. Rev.*, 2016, **45**, 5717–5770.

51 J. W. Kim, V. Augustyn and B. Dunn, *Adv. Energy Mater.*, 2012, **2**, 141–148.

52 X. Wang, G. Li, Z. Chen, V. Augustyn, X. Ma, G. Wang, B. Dunn and Y. Lu, *Adv. Energy Mater.*, 2011, **1**, 1089–1093.

53 J. Come, V. Augustyn, J. W. Kim, P. Rozier, P.-L. Taberna, P. Gogotsi, J. W. Long, B. Dunn and P. Simon, *J. Electrochem. Soc.*, 2014, **161**, A718–A725.

54 C. Zhang, R. Maloney, M. R. Lukatskaya, M. Beidaghi, B. Dyatkin, E. Perre, D. Long, W. Qiao, B. Dunn and Y. Gogotsi, *J. Power Sources*, 2015, **274**, 121–129.

55 Z. Chen, V. Augustyn, X. Jia, Q. Xiao, B. Dunn and Y. Lu, *ACS Nano*, 2012, **6**, 4319–4327.

56 D. Chao, C. Zhu, P. Yang, X. Xia, J. Liu, J. Wang, X. Fan, S. V. Savilov, J. Lin, H. J. Fan and Z. X. Shen, *Nat. Commun.*, 2016, **7**, 12122.

57 A. Sumboja, C. Y. Foo, X. Wang and P. S. Lee, *Adv. Mater.*, 2013, **25**, 2809–2815.